Rock Mechanics and Rock Engineering (2022) 55:169–186
https://doi.org/10.1007/s00603-021-02652-3

ORIGINAL PAPER

Microscopic Modeling of Frictional Response of Smooth Joint Under Normal Cyclic Loading

Qingsheng Bai[1] · Heinz Konietzky[1] · Wengang Dang[2]

Received: 18 February 2021 / Accepted: 18 September 2021 / Published online: 30 September 2021

Abstract

Normal stress changes occur commonly during fault and rock joint rupture, and play a key role in determining frictional behavior and shear stability of these discontinuities. Previous experimental studies of the direct shear test under cyclic normal loads confirm that there exists a phase shift between peak normal stress and peak shear stress, as well as between peak friction coefficient and peak shear stress with shear stress and friction coefficient lagging. However, the underlying physics of this finding is poorly understood. Here, we present a numerical study to investigate the effect of cyclic normal loads on the friction of smooth joints. Our simulations show reasonable agreements with experimental observations, verifying the capability of the proposed model based on the discrete element method. We also investigate the effect of normal loading rate, dynamic amplitude, static normal stress level, shear velocity, and joint stiffness on the frictional behavior of the joint. From a microscopic point of view, we focus on the underlying processes of the phase shift between the peak shear stress (friction coefficient) and peak normal loads. We find that phase shift is related to the changes of the population of slipping and frozen contacts, and also the evolutions of shear force, shear velocity, and shear displacement of individual contacts, in which the macroscopic shear velocity plays a significant role. Inhomogeneous stress distributions near the joint indicate that damage or failure should occur in some contact-scale regions, although which is not directly verified due to the limitations of the presented model. Our work improves the understanding of the physics on how normal load perturbations affect the shear behavior of smooth rock joints.

Keywords Cyclic normal load · Frictional response · Smooth joint · Phase shift · Microscopic physics

Abbreviations

μ [–]	Static friction coefficient
α_s [–]	Relative lagging between peak shear stress and peak normal load
Δts [timesteps]	Shift between the peaks of normal and shear stresses
T [timesteps]	Period of normal stress wave
μ_a [–]	Apparent friction coefficient
R_{pp} [–]	Peak-to-peak ratio of shear stress to normal stress
α_f [–]	Relative lagging between peak friction coefficient and peak normal load

✉ Qingsheng Bai
qingsheng_bai@yahoo.com

[1] Geotechnical Institute, TU Bergakademie Freiberg, Gustav-Zeuner-Straße 1, 09599 Freiberg, Germany

[2] School of Civil Engineering, Sun Yat-Sen University, Zhuhai 519082, China

1 Introduction

Changes in normal stress play a significant role for shear stability and frictional behavior of rock joints and tectonic faults (Dang et al. 2016; Ohnaka 2013; Shreedharan et al. 2019; Xing et al. 2007). Dynamic normal stresses occur during natural or induced earthquakes (Harris 1998; Stein 1999), at subsurface excavations (e.g., blasting, rock bursts, and mining tremors) (Barthwal and van der Baan 2020; Li et al. 2016, 2020; Orlecka-Sikora et al. 2012; Xing and Han 2020), during slip movements on faults in heterogeneous materials, or under specific stress conditions (Bai and Young 2020; Kilgore et al. 2012, 2017). Studies have implied that normal stress changes may impede or promote rupture propagation (Bhat et al. 2004; Duan and Oglesby 2005), depending on the fault geometry and on how fault strength varies in response to the normal stress change (Kilgore et al. 2012). Normal stress change is significant in triggering seismicity. For example, observations have shown that aftershocks tend to occur

in regions of reduced normal stress (Harris 1998). Similarly, fault reactivity usually occurs in areas where normal stress reduction plays an important role (Barthwal and van der Baan 2020; Orlecka-Sikora et al. 2012; Ziegler et al. 2015). However, how normal stress changes affect the dynamic frictional strength of rock joints or faults remains unclear (Shreedharan et al. 2019).

In earthquake engineering and sciences, normal stress step tests, where the normal stress is rapidly changed while the joint is shearing at a constant slip rate, have been widely employed to investigate the effect of normal stress changes on the frictional behavior of joints (Hong and Marone 2005; Kilgore et al. 2012, 2017; Linker and Dieterich 1992; Prakash 1998; Shreedharan et al. 2019). However, the results of these studies differ. Generally, the two following types of frictional responses have been identified (Kilgore et al. 2012; Shreedharan et al., 2019): (1) Experiments conducted by Hobbs and Brady (1985) and Linker and Dieterich (1992) show that a step increase in normal stress causes an instantaneous increase in shear stress, and then, a linear increase is followed by a further exponential increase. This conclusion was confirmed by experiments on Westerly granite (Hong and Marone 2005; Shreedharan et al. 2019; Wang and Scholz 1994) and on gouge layers (Hong and Marone 2005; Mair and Marone 1999). (2) Several studies (Kilgore et al. 2012, 2017) on bare joints found that the shear strength does not immediately increase but evolves gradually, approximately exponentially with ongoing slip until a new steady state is reached. Previous works by Prakash (1998) showed similar behavior for bi-material interfaces consisting of metal blocks under very high normal stresses and slip velocities.

Several studies have focused on how mechanical vibrations affect frictional sliding of fault gouge (Capozza et al. 2009; Giacco et al. 2015; Griffa et al. 2011, 2012, 2013; Johnson et al. 2008). However, only a few studies pay attention to normal stress perturbations. Ferdowsi et al. (2015) identified a critical strain amplitude ($\sim 10^{-6}$) of normal vibration necessary to trigger large slip events. Ferdowsi et al. (2014) also confirmed that induced frictional weakening does not occur if the applied amplitude is below a certain threshold. Shear stress drop usually depends on vibration amplitude (Griffa et al. 2013) and stress state at the time of vibration (Ferdowsi et al. 2015). Capozza et al. (2009) discussed the role of vibration frequency in determining an overall suppression of the macroscopic friction of a granular layer. The defined range of frequencies also depends on vibration amplitude, pressure, and system damping. It is generally recognized that macroscopical friction weakening is controlled by the microscopic evolution of internal structures characterized by contact force networks, coordination number, or particle rearrangements (Ferdowsi et al. 2015; Griffa et al. 2011, 2012). However, such weak perturbations cannot trigger slip of rock joints when gouge is absent (Johnson et al. 2016). Therefore, whether these conclusions can be extrapolated to bare joint systems need to be investigated.

Due to the limitations of the existing shear box devices, only a few studies focus on frictional behavior of rock joints under cyclic normal loads (Dang et al. 2020), especially for larger scale rock joints (Konietzky et al. 2012). Recently, Dang et al. (2016, 2017, 2018, 2020) (Konietzky et al. 2012) performed a series of direct shear tests on large planar joints (30×16 cm) under constant shear velocity and dynamic normal load (DNL) conditions (i.e., constant normal load superimposed by dynamic normal loads). Their experiments show some new findings that have not been observed in traditional direct shear tests (summarized in Appendix). Sobolev et al. (1993, 2016) conducted a series of experiments considering more complex vibrations to investigate the unstable slip of rock joints triggered by elastic impulses (normal and shear velocities, but with energy by several orders of magnitude lower than the energy accumulated by the rock joint). Their observations show that stick–slip can be triggered by a stress impulse when the shear stress is well below the level where stick–slip occurs without the impulse. They also found that the slip lags behind the stroke movement, and that time delay depends on the energy of the triggering.

Particle flow code (PFC) is considered as a preferred choice to simulate rock joint behavior under dynamic loads (herein, cyclic loads) because of its fully dynamic solution to Newton's law of motion (Itasca Consulting Group Inc 2017). Several contact models are available to simulate rock joints in PFC, e.g., the Linear Contact Model (LCM) and the Linear Parallel Bond Model (LPBM). For these two models, joints were simulated by removing bonds of contacts around the intended joint plane or degrading their strength and/or stiffness (Kulatilake et al. 2001; Mehranpour and Kulatilake 2017; Park and Song 2009). However, these two models usually introduce an unrealistic roughness to the joint, because particles on the opposite sides of the intended joint should slide on their perimeters (Lambert and Coll 2014; Mehranpour and Kulatilake 2017). This limitation usually results in unrealistic behavior, such as overestimating the shear strength and producing preliminary dilation (Lambert and Coll 2014; Mehranpour and Kulatilake 2017). Although reducing particle size near the intended joint may overcome this limitation (Kulatilake et al. 2001), this method may increase the computational cost to unpractical levels, especially for smooth joints where the roughness is usually below the micron scale. To solve this shortcoming, the smooth-joint contact model (SJCM) was proposed (Ivars et al. 2011; Pierce et al. 2007). The SJCM simulates the behavior of a planar interface with dilation regardless of the local particle contact orientations along the interface. The contact model enables the two particles to cross each other (i.e., overlap) by sliding along their hypothetical joint plane instead of being

forced to move on their perimeters (Itasca Consulting Group Inc 2017; Ivars et al. 2011). Hence, the model could remove the effect of the inherent roughness of the interface surfaces (Ivars et al. 2011; Lambert and Coll 2014; Mehranpour and Kulatilake 2017), which is relevant to simulate the shear behavior of smooth joints. Therefore, the SJCM is employed in this study. Detailed descriptions of the LCM, LPBM, and SJCM, their capabilities, as well as validation studies, can be found in Cundall and Strack (1979), Itasca Consulting Group Inc (2017), Ivars et al. (2011), Potyondy (2015), and Potyondy and Cundall (2004).

This study is motivated by previously mentioned laboratory investigations and aims at understanding the underlying mechanism of the new findings (see Appendix for detail). After calibration of the mechanical parameters, DEM models are employed to investigate the effect of several factors (normal loading rate, dynamic amplitude, static normal stress level, shear velocity, and joint stiffness) on the shear behavior of smooth joints. Numerical results are compared with experimental observations and verified the capability of the DEM models to appropriately capture variations of shear stress and friction coefficient subjected to DNL. Then, from a microscopic point of view, attention is paid to interpreting the underlying process of phase shift between peak shear stress (friction coefficient) and peak normal load. Stress distributions near the joint are determined. Its potential role in asperity damage and how contact state and shear force affect the stress distribution at the grain size level are analyzed. Possible mechanisms that may cause disagreements between simulations and experiments are discussed. This study deepens the understanding of how perturbations acting in normal direction affect the shear behavior of rock joints.

2 Experimental Observations

In this section, we summarize new findings from the experiments of (Dang et al. 2016, 2017, 2018, 2020) carried out at the Chair for Rock Mechanics at TU Bergakademie Freiberg. The experiments are based on a biaxial direct shear configuration designed to investigate the complex frictional behavior of bare faults under DNL conditions. The experiments consisted of two cement blocks with a size of 300 mm × 160 mm × 150 mm (length/width/height). The maximum asperity amplitude of the shear plane is less than 1.0 mm. In the DNL tests, one block was fixed, and constant shear velocity was applied to the other block. While, in the normal direction, cyclic sinusoidal loads were applied with various amplitudes. Details of the test configuration can be found in our previous publications (Dang et al. 2016, 2017, 2018, 2020; Konietzky et al. 2012). To avoid repeating these published works, we summarize the main experimental results in the Appendix.

Although novel frictional behavior has clearly been identified in lab tests, the physical mechanisms behind are still unclear. Microscopic physics of joint contacts and evolutions of contact states during shearing could be a promising approach to reveal underlying mechanisms; however, such microscopic investigations are usually not feasible via lab investigations, especially for such large-scale tests. In this study, DEM models were employed to reveal fundamental mechanisms underlying these unique observations. It should be noted that this study does not intend to fully duplicate experimental observations but to expand our understanding of microscale frictional processes of smooth joints under DNL conditions.

3 Simulation Methodology

To precisely model the shear behavior and to obtain acceptable calculation time, we use fine particles (with diameters between 0.18 and 0.3 mm) near the joint plane and gradually enlarge the size with distance away from the joint plane. The 2D model consists of 12,712 balls, as shown in Fig. 1. Following the method presented in Mehranpour and Kulatilake (2017), the sample is first separated into two parts based on their relative positions to the intended joint plane. Then, the two blocks are connected by smooth-joint contacts at the joint plane, as shown in Fig. 1. The LPBM is used to simulate the rock blocks, and very high tensile and cohesive strength are assigned to the parallel-bond contacts, since the blocks (rock matrix) did not fail during the laboratory experiments (Dang et al. 2016, 2017). The elastic parameters of the LPBM are obtained by calibrating the elastic modulus (30 GPa) and Poisson's ratio (0.2) of the cement blocks used in the experiment (Dang et al. 2017). Appropriate normal and shear stiffnesses are employed to simulate the elastic behavior near the joint, which are based on Young's modulus and Poisson's ratio of the rock. Table 1 lists the calibrated micro-parameters of the model.

In PFC, a contact is created or activated if the surface gap between the two particles is negative, while a contact is lost or becomes inactive if the surface gap becomes positive (Itasca Consulting Group Inc 2017; Mehranpour and Kulatilake 2017). Therefore, during the shearing, contact creations (positive surface gap becomes negative) and loss (negative surface gap becomes positive) frequently occur if the shear displacement is sufficient (relative to the size of the particles). By default, newly created contacts are usually assigned the LCM. The new linear contact forces the corresponding parent particles (i.e., interlocking particles) to slide on their perimeters but not along the intended joint, resulting in force concentration at the created linear contact (Mehranpour and Kulatilake 2017). This mechanism usually causes an increase in the shear resistance of the joint (Bahaaddini

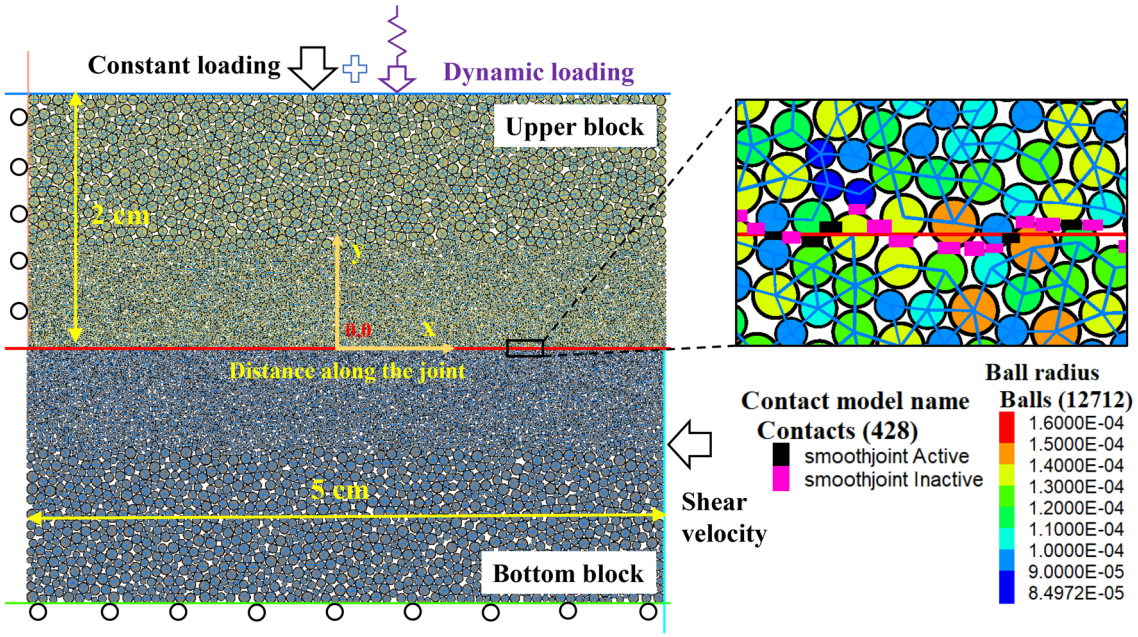

Fig. 1 Numerical model showing boundary conditions, sample dimension, particle size, rock joint, and smooth-joint contacts.

Table 1 Micro-parameters for blocks (rock matrix) and rock joint

Particle properties		Contact bond micro-properties	
LPBM parameters			
Density (kg/m^3)	2500	Bond effective modulus (GPa)	16
Effective modulus (GPa)	16	Bond normal-to-shear stiffness ratio	1.6
Normal-to-shear stiffness ratio	1.6	Tensile strength (MPa)	1000
Friction coefficient	0.7	Cohesion (MPa)	1000
		Friction angle (°)	30
SJCM parameters			
Effective modulus (GPa)	16.0	Friction coefficient	0.33 ± 0.033
Normal-to-shear stiffness ratio	1.6	Joint bond state	Unbonded
Joint radius multiplier	0.6	Large strain flag	Ture

et al. 2013), which cannot reflect the realistic shear behavior of smooth joints. In this study, we use a group behavior function (Itasca Consulting Group Inc 2017) to avoid this problem, which shares a similar idea with the joint plane checking approach (Mehranpour and Kulatilake 2017). This function allows us to filter created contacts whose parent particles belong to the two separated blocks, and these contacts are identified as joint contacts and assigned the SJCM. Newly created contacts whose parent particles belong to a single block are assigned the LPBM.

We calibrated the smooth-joint parameters by reproducing the direct shear tests (Dang et al. 2016, 2017, 2018) with normal loads varying between 1.0 and 7.0 MPa. Figure 2 clearly shows that the shear stress first linearly increases with shear displacement and then gradually changes to nonlinear behavior before reaching the peak stress. Finally, the residual shear stress is nearly identical to the peak shear stress. The static friction coefficient μ is about 0.81 (corresponding to the Mohr–Coulomb theory), as shown in Fig. 2b Both shear behavior and joint strength show a good agreement with laboratory experiments (Dang et al. 2016). We have not calibrated the shear stiffness of the joint (i.e., shear stress–shear displacement curve), because it has a limited effect on shear behavior in relation to DNL (see Sect. 4.5 for detail)

The micro-properties used in the model are listed in Table 1. Stiffness of the SJ contacts is uniformly distributed within the range of $(7.21 \pm 1.54) \times 10^4$ GPa, determined by effective modulus and particle radii (uniform distribution). The friction coefficient of the SJ contacts is also Gaussian distributed with mean and standard deviation of 0.33 and 0.033, respectively. Considering heterogeneity can

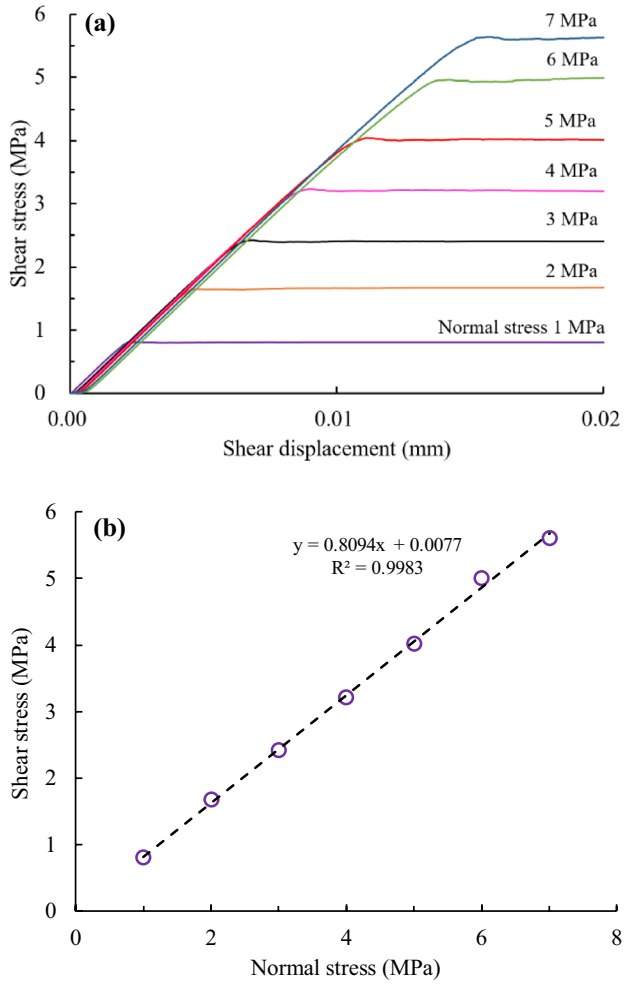

Fig. 2 Numerical calibrations for the direct shear tests. **a** Shear stress versus shear displacement with various normal stresses; **b** shear stress versus normal stress.

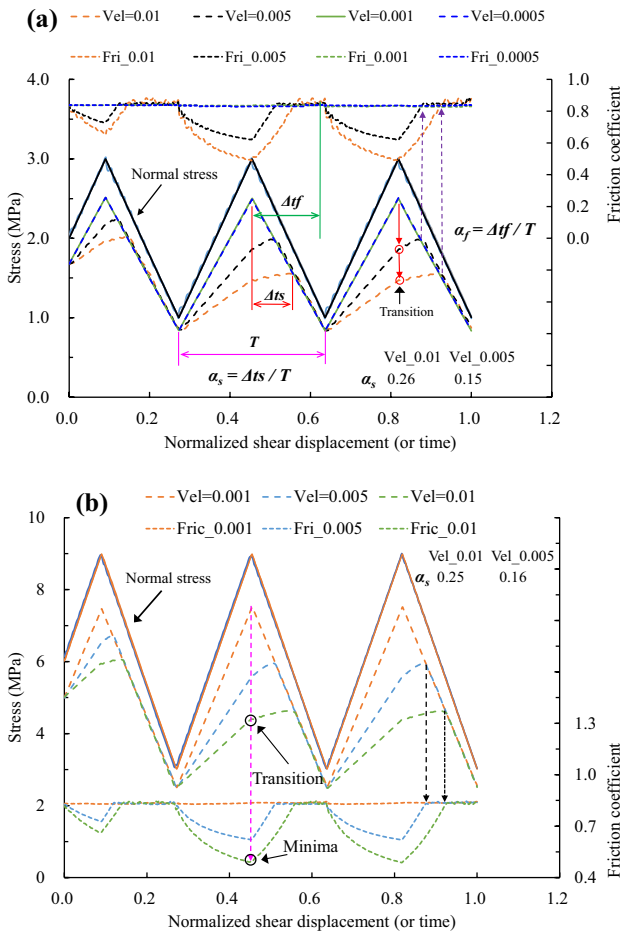

Fig. 3 Normal stress, shear stress, and friction coefficient versus normalized shear displacement (or time) for **a** normal load of 2 MPa and superimposed dynamic load of ± 1 MPa and **b** normal load of 6 MPa and superimposed dynamic load of ± 3 MPa. Solid lines represent normal stress, and dashed lines represent shear stress. Four scenarios are presented in (**a**) with normal loading rates of 0.0005, 0.001, 0.005, and 0.01 m/s. The definition of α_s (relative lagging between peak shear stress and peak normal load) and α_f (relative lagging between peak friction coefficient and peak normal load) is illustrated.

better reflect the reality, because roughness (asperity) heterogeneity (size, height, and the corresponding mechanical parameters) are ubiquitous even for well-prepared smooth joints (Greenwood and Williamson 1966; Müser et al. 2017; Ohnaka 2013).

It should be noted that this study does not intend to fully reproduce the laboratory experiments (a qualitative comparison with experimental results is provided in Sect. 4) but to uncover the underlying physical mechanisms from a microscopic point of view. Therefore, this is a generic model to investigate the frictional behavior of smooth joints under cyclic normal loads and the associated microscopic mechanisms. Although vastly simplified models were employed, numerical results show reasonable agreements with experimental observations (see Sect. 4 for details). Most importantly, numerical simulations boost our understanding of micro-physical processes that dictate the frictional behavior of a smooth joint under DNL conditions.

4 Simulation Results

4.1 Effect of Normal Loading Rate

Figure 3 shows shear stress and friction coefficient versus normalized shear displacement under normal load of 2.0 and 6.0 MPa, with superimposed dynamic pressure of ± 1.0 and ± 3.0 MPa, respectively. For quantitative comparison under different normal load conditions, we normalized the shear displacements (or times) to the maximum values for each scenario. Relatively higher shear stress peaks occur in the first period, which decrease and remain constant in the following periods. Therefore, the analysis focuses on the later periods (i.e., stable periods). It clearly shows that the changing pattern of shear stress is

in phase with the variations of normal load when the normal loading rates are low, e.g., loading rate < 0.001 m/s. If higher loading rates are employed, the peak shear stress lags behind the peak normal stress (i.e., phase shift), which is consistent with experimental results shown in Fig. 18. In this study, we use the relative lagging coefficient α_s to depict the delay of the shear stress. This dimensionless variable is defined as the ratio of shift Δts between the peaks of the normal and shear stresses to the period (T) of the normal stress wave (see Fig. 3a). As the normal loading rates vary from 0.005 to 0.01 m/s, α_s increases from 0.15 to 0.26 and from 0.16 to 0.25 in the two scenarios with different static normal stress, indicating a frequency dependency but static normal stress independence. This observation is consistent with the experimental results, which show that relative shift increases with normal load frequency (i.e., normal loading rate) considering the same shear velocity (Dang et al. 2018), as shown in Fig. 18.

A gradual transition of the shear stress appears after the normal stress passes into the unloading phase, as shown in Fig. 3. After the peak value, the shear stress decreases to a minimum with the same rate as the normal stress, meaning no time lag in the unloading stages, which agrees with the experimental observations (Fig. 18). The maximum shear strength also depends on the normal loading rate (frequency in the experiments); it reduces from 1.99 to 1.55 MPa and from 5.95 to 4.43 MPa in the two scenarios as the normal loading rate increases from 0.005 to 0.01 m/s. Lab experiments also show that the minima of μ_a and α_s depend on normal loading frequency (Fig. 18).

In scenarios with low normal loading rates, μ_a remains almost constant (Fig. 3), indicating proportional variation between normal and shear stress. The maxima of μ_a are 0.839 and 0.834 for the two scenarios, which are slightly higher than μ at the same normal stress levels (see Fig. 2b). In situations with higher normal loading rates, μ_a gradually decreases in the loading stages and reaches the minimum at the point of peak normal stress, as shown in Fig. 3. It rises at a higher rate in the unloading stages and reaches the maxima at troughs of the DNL. The slower rising rate of the shear stress attributes to the decrease of μ_a in the loading stage, while the time shift between normal and shear stresses results in a gradual increase. μ_a then remains unchanged in the unloading stages. Experiments also show that μ_a always maximizes at the trough of the normal stress curve (Fig. 18). The minima of μ_a decrease from 0.61 to 0.49 when normal loading rate increases from 0.005 to 0.01 m/s (Fig. 3a), indicating normal loading rate (or frequency) dependence, and laboratory tests document the same behavior (Fig. 18). Figure 3b demonstrates the same changes in the minima of μ_a (from 0.62 to 0.49), which indicates static normal stress level and dynamic amplitude independence.

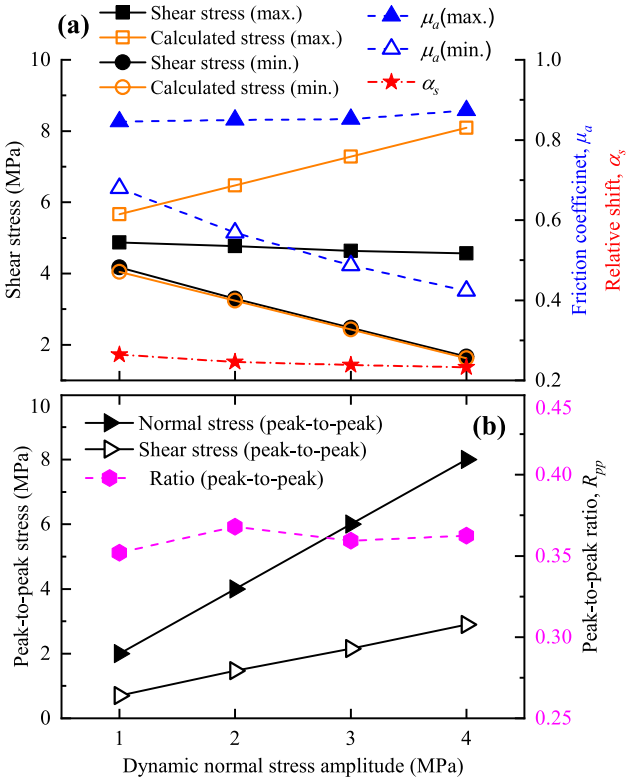

Fig. 4 Effect of the dynamic normal stress amplitude (with static normal stress of 6 MPa) on **a** shear stress, apparent friction coefficient (μ_a) and relative shift between the peak shear stress and peak normal stress (α_s), and **b** peak-to-peak stress and peak-to-peak ratio (R_{pp}, the ratio between peak shear stress and peak normal stress). For comparison, the 'static' shear stress (multiplying the corresponding normal stress with the static friction coefficient) is plotted in (**a**). All the simulations use the same normal loading rate

4.2 Effect of Dynamic Normal Stress Amplitude

Figure 4 illustrates the effects of dynamic normal stress amplitude on maximum and minimum shear stress, μ_a, and α_s. Both maximum and minimum shear stress decrease as dynamic normal stress amplitude increases, but the maximum shear stress shows a much slower rate than that of the minimum. It is not difficult to explain the decline of the minimum shear stress, since the minimum normal load also declines with dynamic normal load amplitude. Similarly, an increase in maximum shear stress should be observed, because the maximum of normal stress also rises as the normal stress amplitude increases. These observations agree with lab tests (Fig. 16). The dynamics in terms of physics of the rock joint should be responsible for this 'abnormal' change (see Sect. 5).

Figure 4 also shows the 'static' shear stress obtained by multiplying the corresponding normal pressure with μ (Fig. 2b), for comparison with the dynamic ones. It clearly shows that the minimum shear stresses under dynamic

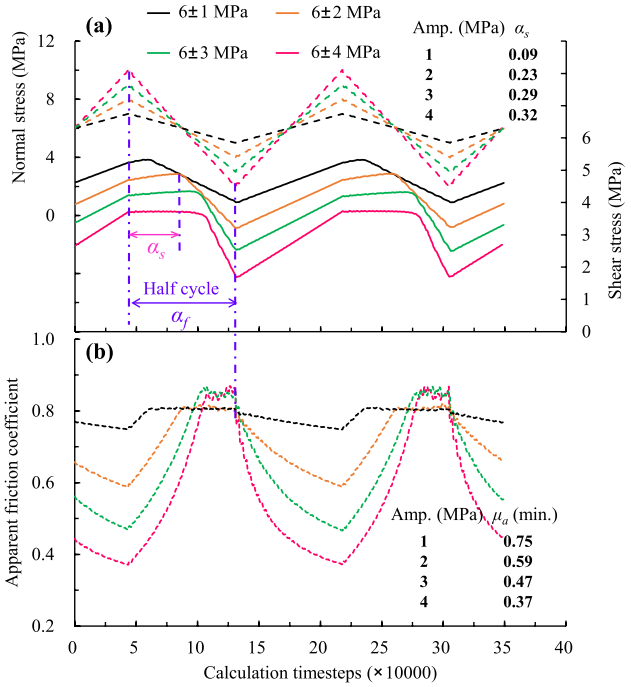

Fig. 5 Effect of dynamic impact amplitude with the same frequency on shear behavior of rock joint. **a** Normal and shear stress versus calculation timesteps (dashed lines signify normal stress, and solid lines signify shear stress). **b** Apparent friction coefficient (μ_a) versus timesteps for different dynamic impact amplitudes. Stable stages are taken, and the starting time is shifted to zero. 6 ± 3 MPa signifies the normal load varies ± 3 MPa around the static normal stress of 6 MPa. The relative shift between peak shear stress and peak normal stress (α_s) and the minimum of μ_a for each scenario are provided in (**a**) and (**b**), respectively.

perturbation are almost identical to the static ones. Lab experiments also witness the same maxima of μ_a near troughs of DNL (Fig. 16), indicating that the minima of shear stress are independent of DNL. However, the maximum shear stresses under dynamic conditions are lower than the static ones; and the differences between them increase linearly with increasing dynamic amplitudes. The minimum shear stress is always synchronous with the minimum normal load (Fig. 5), making it equal to the static one. However, the maximum shear stress lags behind the maximum normal stress when some conditions are satisfied. Thus, the shear stress cannot further increase to the corresponding static value in the normal stress unloading stage. With higher normal pressures, longer shear distances are required to activate shear resistance, which is discussed in detail in the following section.

The maximum value of μ_a shows a slight increase (from 0.85 to 0.87) as the dynamic amplitude increases (Fig. 4). The maxima of μ_a occur in the unloading stages, where shear stresses synchronously decrease with decreasing normal stress (see Fig. 3), leading to the independence of normal stress. However, the minima of μ_a monotonously decrease (from 0.68 to 0.42) as the dynamic amplitude increases. Experimental tests show a similar variation of μ_a in relation to normal stress amplitudes. Dang et al. (2017) found constant values for the maxima of μ_a and a decrease in the minima of μ_a with increasing dynamic normal stress amplitude (see Fig. 16). A variation of maximum and minimum shear stress also leads to relatively low but constant values (~0.36) of peak-to-peak ratios R_{pp} of shear stress to normal stress, as shown in Fig. 4b. α_s shows a slight decrease (within 12%) with an increase in dynamic normal load amplitudes (Fig. 4a).

In Fig. 4, we use the same normal loading rates (i.e., different frequencies), while laboratory experiments usually employed identical frequencies (Fig. 16) when analyzing the amplitude effects. We re-run the cases documented in Fig. 4, applying the same frequency (i.e., different normal loading rates). We observe nearly trapezoidal signals for the shear stress, as shown in Fig. 5, similar to the experimental results (Fig. 16). After the transition points (Fig. 3), the shear stress slowly increases as the normal stress decreases, but μ_a quickly rises. Figures 4 and 5 suggest that the variation of μ_a in unloading stages is independent of normal impact amplitude and frequency (i.e., unloading rate). α_s increases with increasing dynamic normal load amplitudes (Fig. 5a), which is contradictory to the results shown in Fig. 4, indicating a loading rate (or frequency) dependence of the relative time shift. Laboratory tests witness similar changes (Fig. 16), where α_s increases from 0.105 to 0.19 when dynamic amplitudes vary between 0.625 and 1.25 MPa. The minima of μ_a decrease with increasing amplitude, but the maxima remain constant, as shown in Fig. 5b. μ_a maximizes near the troughs of the normal stress waves. The relative lagging between peak friction coefficient and peak normal load α_f (see Fig. 5a) is nearly constant, i.e., 0.5. These observations are also coincident with laboratory experiments (Fig. 16).

4.3 Effect of Static Normal Stress Level

The static normal stress level has a limited effect on the maxima of μ_a, which vary between 0.88 and 0.82 as the normal stress increases from 2.0 to 7.0 MPa with the same dynamic amplitude of 1 MPa, as shown in Fig. 6a. R_{pp} also varies within a limited range (± 10%), as shown in Fig. 6b. It should be noted that, in these scenarios, the dynamic shear stress varies on the basis of stable shear stresses, which are determined by static normal stress and μ. That means the dynamic shear stress (induced by dynamic normal load) only contributes to a part of the maximum shear stress, and its contributions decrease with increasing static normal stress level. This character leads to increasing the minima of μ_a with increasing normal stress levels (Fig. 6a).

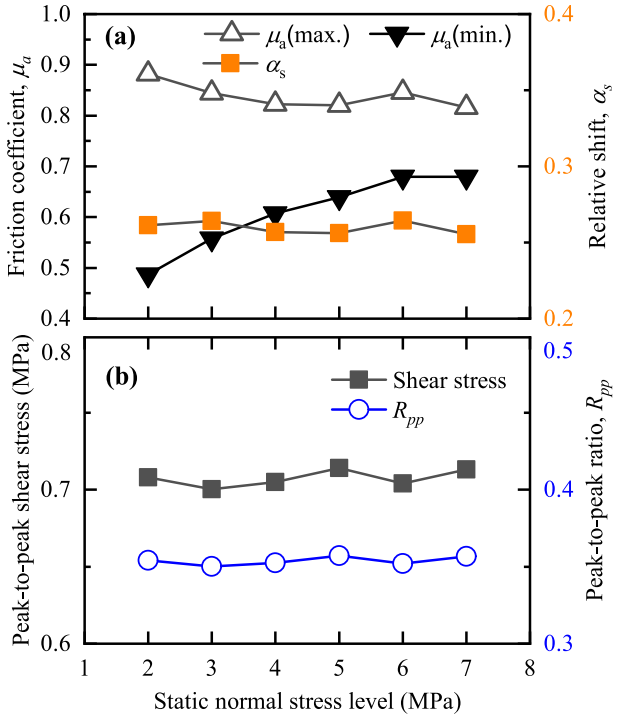

Fig. 6 Effect of static normal stress level on **a** minima and maxima of apparent friction coefficient (μ_a) and relative shift (α_s), and **b** peak-to-peak shear stress and peak-to-peak ratio (R_{pp}) with dynamic impact amplitude of 2 MPa.

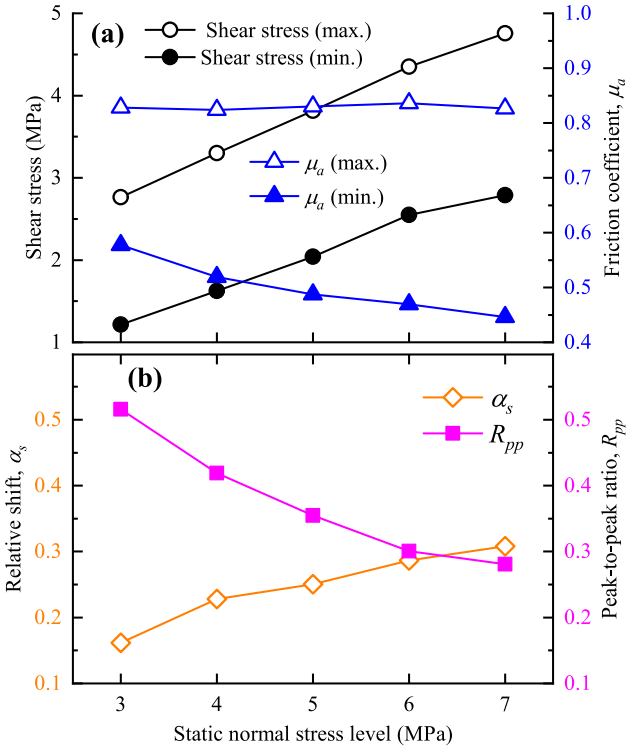

Fig. 7 Effect of static normal stress level (with dynamic amplitude half of the normal stress while using the same wave frequency) on **a** shear stress, apparent friction coefficient (μ_a,), and **b** peak-to-peak ratio (R_{pp}) and relative shift between peak shear stress and peak normal stress (α_s).

α_s remains nearly constant (~0.26), indicating a static normal stress level independence, because we employ the same dynamic amplitude, shear velocity, and normal loading rate in these simulations. The peak-to-peak shear stress shows slight changes (~0.71 MPa). As a result, R_{pp} is much lower (0.35) than μ (0.81). The dynamic shear stress change is less than half of that under quasi-static conditions. This observation rationalizes the fact that the shear resistance has not been entirely activated before the dynamic normal stress decreases (unloading phase).

To allow a direct comparison with experiments, we varied the dynamic amplitudes to half of the static normal stress level but using the same frequency (i.e., different normal loading rates). Figure 7 shows the corresponding plots for shear stresses, apparent friction coefficient, and relative shift versus the static normal stress level. The maximum value of μ_a remains nearly constant (~0.825, the same as the quasi-static value), but the minima decrease with increasing normal stress level. α_s rises from 0.16 to 0.31 with increasing normal stress levels, which is quantitatively consistent with experimental results (Dang et al. 2016). They found that α_s increases from 0.11 to 0.25 as the static normal load level enlarges from 30 to 180 kN with dynamic amplitudes equaling to a half of the static load level (Fig. 8 in their paper). R_{pp} decreases from 0.52 to 0.28 with increasing normal stress. This tendency is consistent with laboratory observations (Dang et al. 2016), where they found R_{pp} decreases from 0.23 to 0.08 as the static normal stress level increases from 15 to 360 kN (Fig. 6a in their paper). The disagreement in quantity may result from different shear velocities and different normal frequencies in these two studies.

4.4 Effect of Shear Velocity

Similar to the experiments (Fig. 17), numerical simulations also show that shear strength, apparent friction coefficient, and the relative shift depends on the relation between shear velocity and normal load frequency. Figure 8a shows that the evolution of μ_a depends on shear velocity. For the case with the highest shear rate (e.g., 0.01 m/s), μ_a remains unchanged during the simulation, indicating that high shear velocity can sufficiently activate the shear resistance of the joint. Therefore, the maxima of the shear stress increase from 2.73 to 8.37 MPa as the shear velocity rises from 0.0001 to 0.01 m/s, as shown in Fig. 8b. The corresponding R_{pp} also increases. When the shear velocity is slower, shear stress increases with a relatively low rate in the loading stage, and continues to grow at the beginning of the unloading stage. This evolution

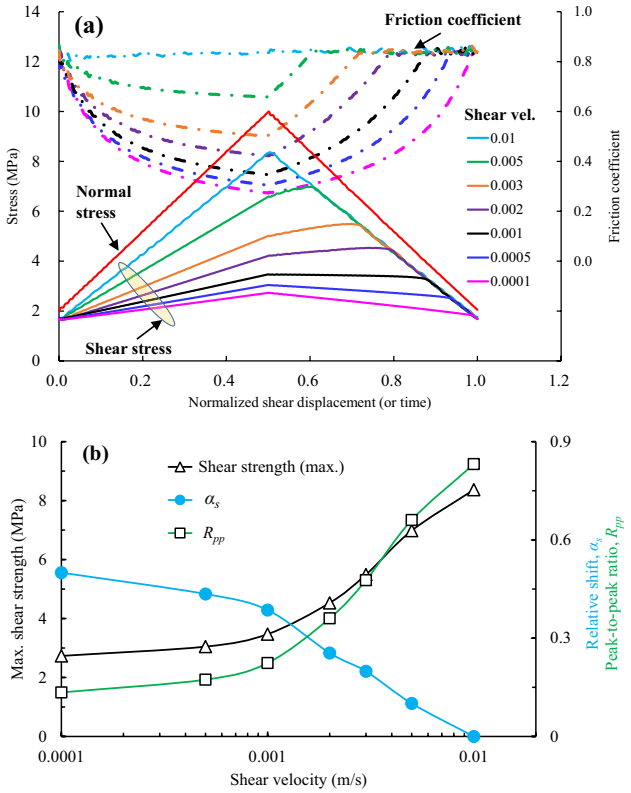

Fig. 8 **a** Normal stress, shear stress, and apparent friction coefficient versus normalized shear displacement (or time) for different shear velocities (note that normal stresses are identical), and **b** effect of shear velocity on maximum shear strength, relative shift (α_s), and peak-to-peak ratio (R_{pp})

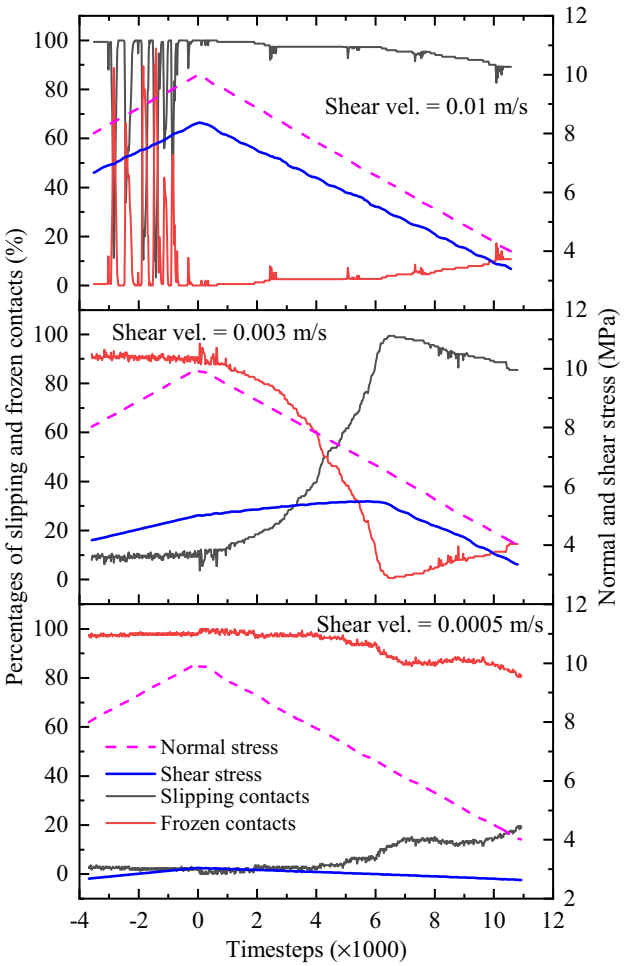

Fig. 9 Effect of shear velocity (0.01 m/s, 0.003 m/s, and 0.0005 m/s) on shear stress changes associated with the evolution of the population of slipping and frozen contacts. Timesteps are shifted to the moment of the maxima of the normal stress (10 MPa)

causes the maximum shear stress lagging behind the peak normal stress, and α_s increases as the shear velocity reduces, as shown in Fig. 8b. When the shear velocity is below 0.001 m/s, a different shear stress curve occurs: shear stress drops during unloading but with a lower rate compared to the loading stage. Therefore, in these scenarios, shear stress maximizes at the point of peak normal loads. These numerical results are consistent with experimental observations (Fig. 17).

μ_a presents the same changing pattern in relation to the normalized shear displacement. It minimizes at the point of peak normal stress, and then increases in the unloading stage at a faster rate compared to the loading stage, as shown in Fig. 8a. μ_a maximizes and remains constant after points of peak shear stress. If the shear velocity is extremely low, e.g., 0.0001 m/s, μ_a reaches the maxima (quasi-static value) at the wave trough of normal stress, indicating that $\alpha_f = 0.5$ (Fig. 8a). For the lowest shear velocity, α_s also equals to half of the period of the normal stress wave. We also note that the minima of μ_a increase with increasing slip velocity (Fig. 8a). All these observations correspond to the experiments (Dang et al. 2016, 2018), as shown in Fig. 17.

The slip behavior of the joint contacts varies under different shear velocities, which might be the intrinsic mechanism that produces different shear responses. Figure 9 summarizes the results by plotting shear stress as well as slipping and frozen contacts versus the calculation timesteps for three different shear velocities (i.e., 0.0005, 0.003, and 0.01 m/s). The Coulomb criterion determines the state of a contact. In this study, a frozen contact means that the shear force applied to the SJ contact is smaller than the shear strength (i.e., normal force multiplied by the friction coefficient), while a slipping contact signifies that the shear force exceeds the shear strength, i.e., shear force would not increase with the shear displacement. For the case with low shear velocity (0.0005 m/s), frozen (i.e., non-slip) contacts predominate the shear behavior of the joint. The population of frozen contacts remains at a high level in the loading stage, as well as at the beginning of the unloading stage, as shown in Fig. 9. It begins to decrease with a low rate when the normal

stress is below 6.7 MPa. In this case, we observe extremely low shear slip (due to the low shear velocity), as shown in Fig. 10a, which determines the small increase of the shear stress during the vibration, because the shear stress is linearly proportional to the shear displacement according to the Coulomb-slip theory if one contact is in the frozen state. Therefore, normal stress change dominates the evolution of shear stress, while shear slip plays a minor role. Figure 10a also shows the high heterogeneity of slip displacement due to the inhomogeneity of the shear stiffness and friction coefficient of the contacts.

For a high shear velocity (0.01 m/s), the number of slipping and frozen contacts is approximately constant in the loading stage and also at the beginning of the unloading stage, as shown in Fig. 9. This indicates that most of the contacts are slipping during the shearing process (i.e., maximum shear strength is reached for individual contacts under the actual normal force), as shown in Fig. 9. Therefore, the macroscopic shear stress evolves synchronously with the change in normal stress. However, the population of the slipping contacts fluctuates severely as the normal stress approaches the peak value, suggesting a small number of contacts switch their states between slipping and frozen, accompanied by abrupt changes in slip velocity (see Sect. 5.1 for more details). The number of slipping contacts decreases slightly when the normal stress is below 6 MPa. Therefore, in this case, the normal pressure also plays the leading role in the shear stress evolution, because slipping would not contribute to the variation of the shear stress for slipping contacts. Shear displacements at contacts are distributed homogeneously along the rock joint, indicating that most of the contacts move simultaneously along the joint. Therefore, the population of slipping contacts shows minor fluctuation (Fig. 9).

However, for the case with a shear velocity of 0.03 m/s, the population of the slipping contacts slightly increases as peak normal pressure is reached. Then, the number of slipping contacts increases significantly in the unloading stage, with shear stress gradually rising to the peak value. As normal stress reduces, it begins to drop again, leading to a decrease in shear stress. The frozen (non-slipping) contacts show an inverse behavior, as can be seen in Fig. 9. These observations suggest that most of the contacts are near the critical state in the loading stage at low shear velocity. During unloading, the shear stress exceeds the shear strength; thus, a large number of these contacts begin to slip. The shear forces slightly increase as they switch from critical state to slipping state. The decrease in normal stress also plays a role in the slow increase in shear stress beyond the peak point of the normal stress. After that, a majority of the contacts remain slipping; their shear strength is determined by the normal stress imposed, i.e., shear stress drops proportionally to the normal load.

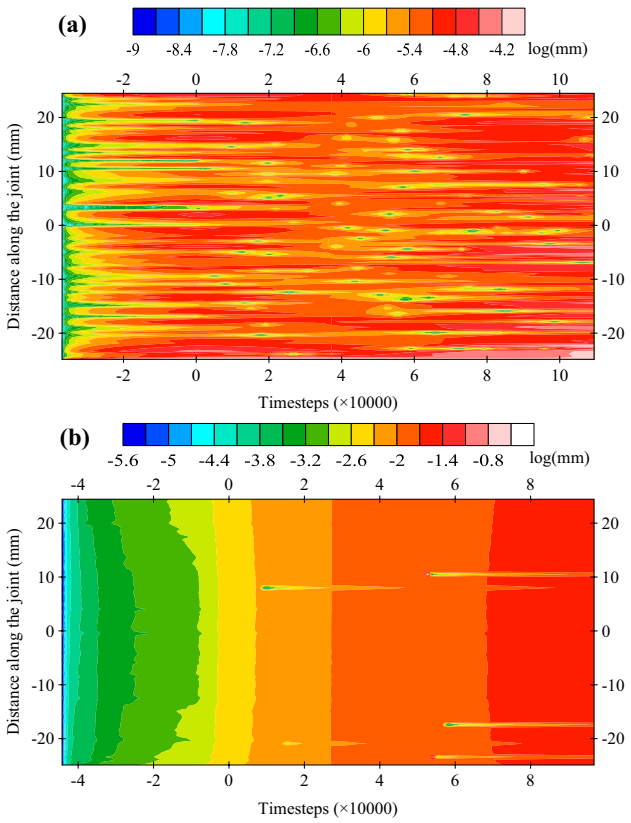

Fig. 10 Evolution of the contact slip displacement with ongoing calculation timesteps for shear velocity of **a** 0.0005 m/s and **b** 0.01 m/s. Timesteps are shifted to the moment of the maxima of normal stress (10 MPa).

4.5 Effect of Joint Stiffness

Normal stiffness of the rock joint has a limited effect on shear strength, α_s, R_{pp}, and the maximum and minimum value of μ_a, as shown in Fig. 11. With increasing normal stiffness, the parameters mentioned above almost keep constant (within 8%), indicating stiffness independence.

Figure 11b documents the behavior of these parameters versus the ratio between normal and shear stiffness. It is noticed that the minimum shear strength approximately remains constant. The maximum shear strength slightly drops when the ratio is larger than 10. Accordingly, R_{pp} shows the same tendency as the maximum shear strength. The maxima of u_a slightly change, while the minima show a decreasing trend when the stiffness ratio is bigger than 10. The relative shift keeps constant (~0.145) when the stiffness ratio is smaller than 10, but gradually increases to 0.22 when the stiffness ratio is larger than 10. Figure 11b clearly shows that a higher stiffness ratio (> 10) plays some role in shear behavior under dynamic normal loads. However, the underlying mechanism needs to be investigated in future.

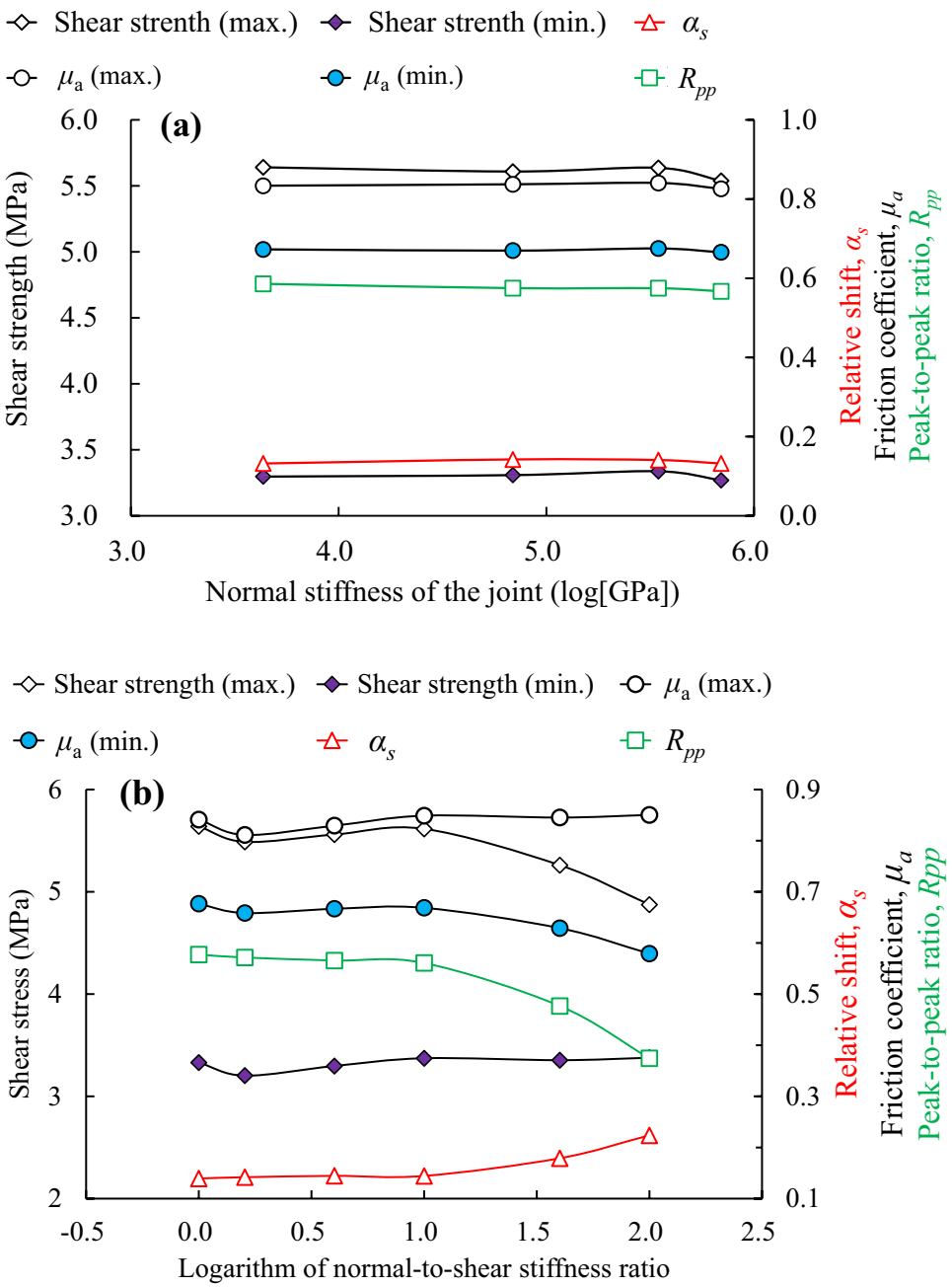

Fig. 11 Effect of joint stiffness on shear strength, relative shift (α_s), peak-to-peak ratio (R_{pp}), and apparent friction coefficient (μ_a). **a** Normal stiffness varies between 4330 and 693000 GPa with a constant ratio of 1.6 between normal and shear stiffness, and **b** ratio between normal and shear stiffness varies between 1 and 100 with a constant normal stiffness of 4330 GPa

5 Discussion

5.1 Micro-physics of the Phase Shift

In this section, we try to interpret the physics of the phase shift (α_s) during the dynamic loading from a microscopic point of view. Figure 12 shows the evolution of shear velocity, shear displacement, and shear force of individual contacts together with macroscopic normal stress, shear stress, apparent friction coefficient, and the population of slipping and frozen contacts. In this case, a constant shear velocity of 0.03 m/s is applied. The shear velocity of the contacts varies in a wide range (four orders of magnitude), from $10^{-5.6}$ to $10^{-1.6}$ m/s. We consider contacts with very low shear velocity as frozen. On these contacts, the shear force is below the shear resistance under the imposed normal stress. Therefore, on these contacts, shear force increases with slip displacement. While contacts with higher shear velocity are slipping, and their shear force is independent on the shear slip but determined by the applied normal force. The normal stress determines the slip velocity at the contacts, which can be separated into three stages. These stages correspond to different features of the shear and normal stresses, as shown in Fig. 12.

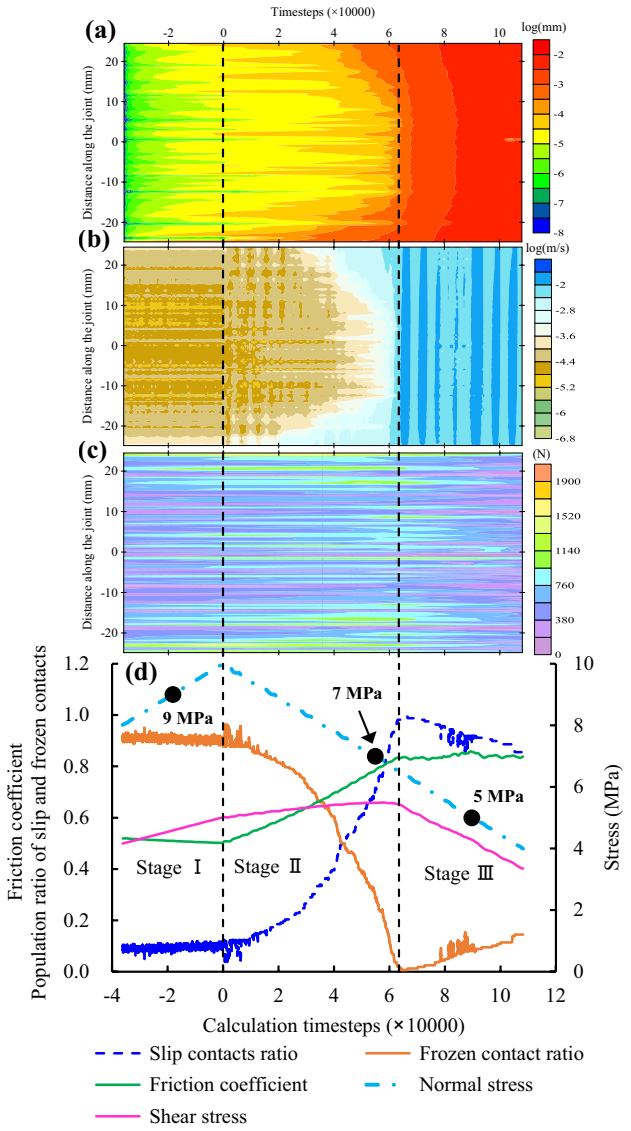

Fig. 12 Evolution of microscopic parameters under dynamic normal stress and a shear velocity of 0.003 m/s. **a** Shear displacement, **b** relative shear velocity, **c** shear force, and **d** normal and shear stress, apparent friction coefficient, as well as frozen and slipping contact ratios versus calculation timesteps. Timesteps are shifted to the moment of the maximum normal stress (10 MPa)

In the loading stage (Stage I), the population of the slipping contacts stays at a low level, slowly increasing with normal load. Both the increase of normal stress (Fig. 12d) and shear displacement (Fig. 12a) contribute to increasing shear force on these frozen contacts. Heterogeneity of shear velocity (Fig. 12b) and displacement (Fig. 12a) along the rock joint are observed, which corresponds to the fluctuations of the shear force (Fig. 12c). There are segments with low shear velocity along the joint, usually producing relatively high shear forces, as shown in Fig. 12c. The heterogeneity of stiffness (Gaussian distribution) and friction coefficient (uniform distribution) dominate the inhomogeneity of shear velocity and shear force. As shearing continues, shear displacement increments occur on more contacts, as shown in Fig. 12a. Therefore, the shear force also increases on these contacts, resulting in increasing shear stresses.

In Stage II, the normal stress decreases, while the shear stress continues to increase but at a slower rate, as shown in Fig. 12d. Reduction of normal stress and shear displacement increments play opposite roles in shear stress growth. Normal stress reduction decreases the shear force of individual contacts for slipping as well as the number of frozen contacts, while shear displacement increment increases the shear force at frozen contacts. This process dominates at the beginning of this stage, since frozen contacts account for the majority. Obviously, shear displacement increments are predominant in this stage, because shear force growth takes place on most of the contacts, as can be seen in Fig. 12c. Unloading decreases the shear resistance, but shear displacement increments increase the shear stress. Therefore, more contacts switch to the slipping state (Fig. 12d). Populations of slipping contacts and shear velocity continuously increase in this stage. Pronounced heterogeneity of shear velocity is observed in this stage, especially when unloading starts. This may be due to the frequent switch of individual contacts between frozen and slipping state. The fluctuation of the population (Fig. 12d) supports this argumentation.

Homogeneous slipping occurs along the joint in Stage III by further unloading, as documented in Figs. 10b and 12a. In this stage, the normal stress directly determines the shear stress of the joint, because most of the contacts are now slipping (Fig. 12d). As a result, the shear displacement increments play only a minor role, since shear force on slipping contacts is independent of shear displacement. This explains why shear stress drops proportionally to normal stress (Fig. 12d). Contacts with high shear force gradually decrease with decreasing normal load (Fig. 12c), also supporting this explanation.

For high shear velocity (e.g., 0.1 m/s), the normal stress plays a primary role in shear stress changes, because most of the contacts are slipping (Fig. 9), independent from shear displacement. Due to the high shear velocity (Fig. 13b) and shear displacement (Fig. 10b), most of the contacts are slipping. These contacts could fully mobilize their shear strength, producing the highest shear strength under the applied normal stress, i.e., μ_a reaches the peak value and remains constant during the dynamic loading, as shown in Fig. 8a.

For low shear velocity (e.g., 0.0005 m/s), the normal stress also plays the primary role in shear stress changes, however, attributed to different physics. In this case, the shear velocity is so low (less than 4×10^{-4} m/s, as shown in Fig. 13a) that a limited shear displacement is produced during the perturbation, as shown in Fig. 10a. Therefore,

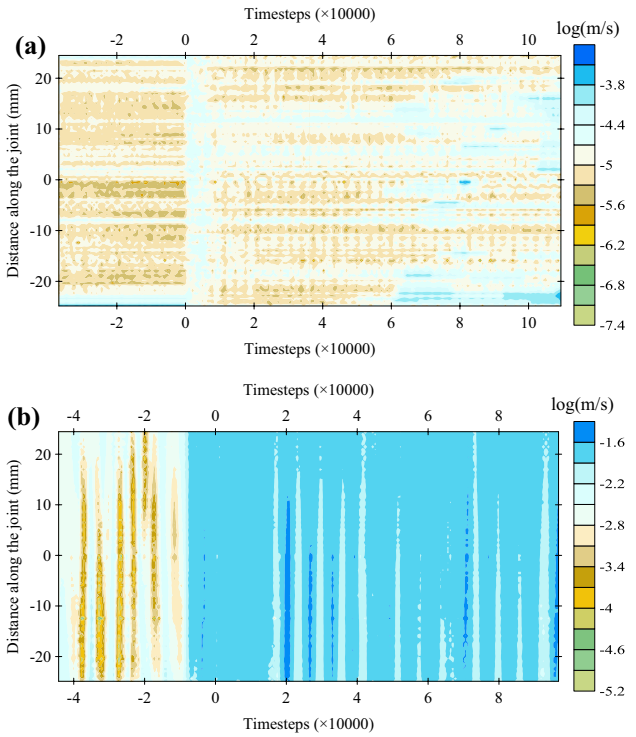

Fig. 13 Evolution of contact shear velocity with ongoing calculation timesteps for shear velocity of **a** 0.0005 m/s and **b** 0.01 m/s. Timesteps are shifted to the moment of maximum normal stress (10 MPa).

shear displacement increments contribute a little to shear stress growth compared with normal stress variation. As the shear displacement accumulates, shear force also increases on these contacts. Consequently, a small number of contacts switch to the slipping state (Fig. 9). This mechanism also causes μ_a to recover to the maximum value preceding the unloading to the basic level, as shown in Fig. 8a.

5.2 Stress Redistribution Near the Rock Joint

Stress redistributions near the rock joint is an important indicator to investigate the damage and failure of the rock block. The minimum principal stress (compression has negative signs) distribution near the joint is shown in Fig. 14. Generally, stress is a continuum quantity and, therefore, does not exist at particles in granular media. Averaging procedures on numbers of particles within a finite cell are usually necessary to obtain the averaged stress (Fortin et al. 2003). However, here, we focus on the induced stress by the SJ contact during shearing at the microscale; therefore, particle stress tensor is calculated by volume average of summing up contact reactions acting at the particle (Itasca Consulting Group Inc 2017), as shown in Fig. 15a. Figure 14 clearly shows that stress is heterogeneously distributed in the rock blocks, especially near the joint. Stress concentrations occur at the boundaries of the blocks where shear velocity and fixed boundaries are applied, respectively. Continuum models demonstrate similar stress concentrations in these regions (Dang et al. 2020). Stress concentrations usually occur in areas with frozen contacts for scenarios with high normal stress, as shown in Fig. 14a, b (see Fig. 14d for detail). Low stresses are always accompanied by slipping contacts or locations where joint detachments occur. However, for the scenario with low normal pressure (Fig. 14c), relative high stresses also appear at locations where contacts slip, while contact detachments are always connected with relatively low stresses (see Fig. 14d for detail).

In fact, it is found that shear forces of the SJ contacts determine the stress distributions near them to some extend. Figure 15 shows a positive correlation between the shear force and the corresponding minimum principal stress on the parent particles (Fig. 15a). However, the data are scattered, which may be attributed to the inhomogeneity of SJ contacts and rock blocks. Nevertheless, the magnitude of the minimum principal stress shows little correlation with the state of the SJ contacts (frozen or slipping).

The minimum principal stress near the rock joint decreases as the normal stress drops. Nonetheless, the maximum value of these principal stresses exceeds the strength of the material (19.1 MPa (Dang et al. 2016)). Contacts are usually isolated distributed at the microscopic scale (Greenwood and Williamson 1966; Shreedharan et al. 2019), as also shown in this study. Thus, some asperities meet the condition of unconfined compressive loading. Consequently, damage or failure should occur at some contact locations where the compressive stress exceeds the material strength. Extremely high strength is assigned to the contacts in our models; therefore, damage could not be observed on the contacts and the particles (rigid bodies), although mild wear occurs in the experiments (Dang et al. 2016, 2017). Stress heterogeneity-induced damage or failure near the rock joint will be an essential question for future investigations.

5.3 Limitations of the Numerical Simulations

Due to the computational limitations, in this study, we employ 2D small-scale models to simulate 3D large-scale experiments. However, this simplification does not affect general conclusions, since 2D numerical simulations can be successfully employed to reproduce 3D direct shear experiments, e.g., (Bahaaddini et al. 2013; Mehranpour and Kulatilake 2017; Saadat and Taheri 2020; Tang et al. 2020). Quantitative comparison with experiments is not available due to the inconsistent shear stiffness, but numerical simulations successfully reproduce relations between shear stress and apparent friction coefficient with respect to DNL.

The presented simulations demonstrate that both shear stress and apparent friction coefficient show cyclic behavior

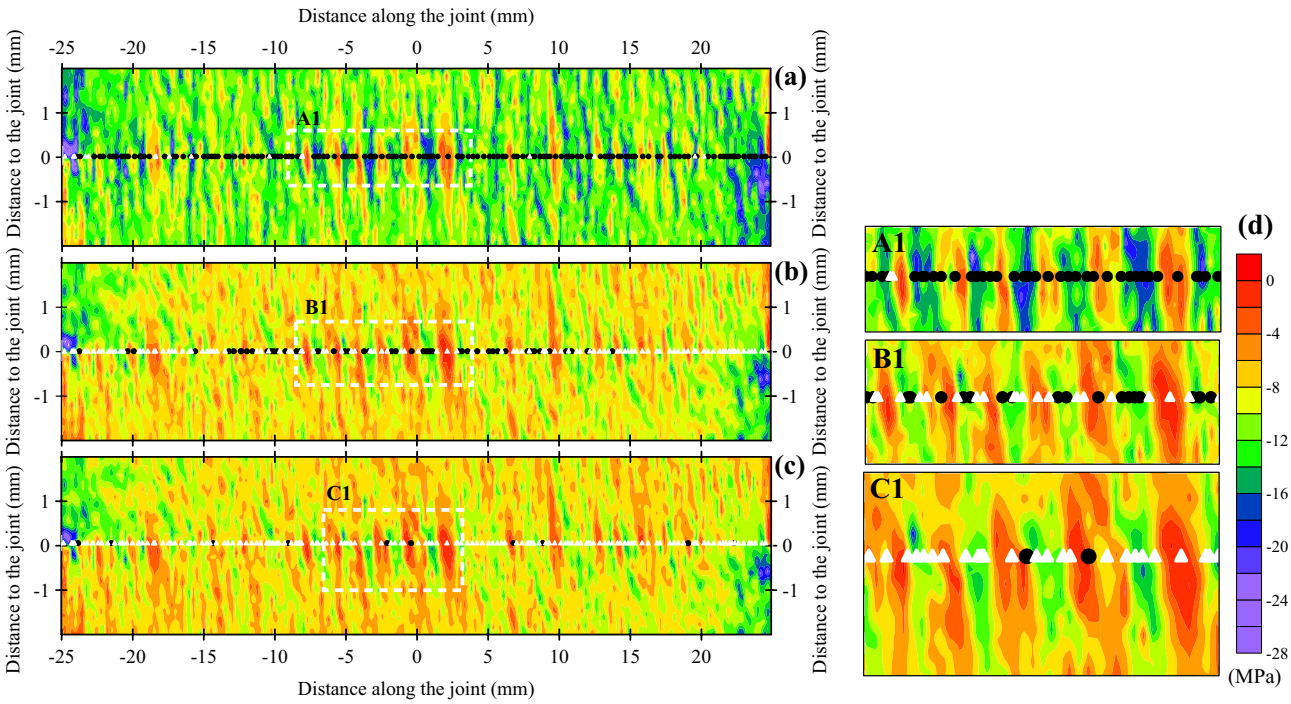

Fig. 14 Minimum principal stress distributions near the rock joint (negative values signify compression) for the scenarios with normal stress for **a** 9 MPa (before peak normal load), **b** 7 MPa, and **c** 5 MPa. See Fig. 12 to identify the corresponding points in time (black dots). **d** Magnifications of interesting regions for the three scenarios. Black circles signify frozen contacts, and white triangles signify slipping contacts.

following the normal load imposed. The maxima of shear stress and μ_a lag behind the peak normal stress. The minima and maxima of μ_a always occur at the crest and trough of the normal stress wave, respectively. α_f is nearly constant (about half the period), especially for cases with low shear velocity and/or high normal loading rate. All these observations closely match those obtained in the laboratory (Dang et al. 2016, 2017, 2018, 2020) (see Appendix for detail), which indicates the capability of the model to appropriately capture the frictional joint behavior in a realistic manner. However, we also find some disagreements between experiments and simulations presented here. For example, our model overestimates R_{pp} when analyzing the effect of static normal stress level (Fig. 4b), while experiments show that it decreases with increasing amplitude (Dang et al. 2018). The following factors may contribute to these disagreements.

In the DEM models, we employ the sawtooth normal stress wave to approximate the sinusoidal excitation used in the experiments. Therefore, normal stress perturbations in our model are produced by constant loading rate, while sinusoidal-like waves usually produce changing loading rates in the lab tests. Experiments (Dang et al. 2018) and simulations presented herein have shown that normal loading rate (i.e., normal loading frequency) plays an essential role for the minima of μ_a, α_s, and peak shear stress (Fig. 18).

Real contact area growth usually occurs with contact aging, shearing, and normal stress increasing (Dieterich and Kilgore 1994; Stesky and Hannan 1987). During shearing or change of normal stress, joint contacts detach and re-attach, as well as rejuvenate between existing and created asperities (Dieterich and Kilgore 1994; Rubinstein et al. 2006; Shreedharan et al. 2019; Stesky and Hannan 1987). Besides, the strength of the contacts usually decreases progressively during shearing (Li et al. 2011; Stesky and Hannan 1987), but can recover with ongoing shear displacement (Ben-David et al. 2010; Dieterich and Kilgore 1994). All these microscopic processes affect the macroscopic shear behavior of the joint. While a simplified numerical model is used in this study, hence evolution of asperity-scale physics is not included. The next challenge is to find an effective approach to well describe the evolution of these micro-processes, e.g., evolution of contact population, area, rejuvenation, strength, etc.

Experiments have proven that gouge material plays a significant role in dynamically triggered slip under shear conditions. Gouge material, phase lag, and frictional strength are all affected by frequency and amplitude of the dynamic loads (Capozza et al. 2009; Johnson et al. 2008; Savage and Marone 2007). Slight wear was also observed in our experiments (Dang et al. 2016, 2017), and a small amount of gouge

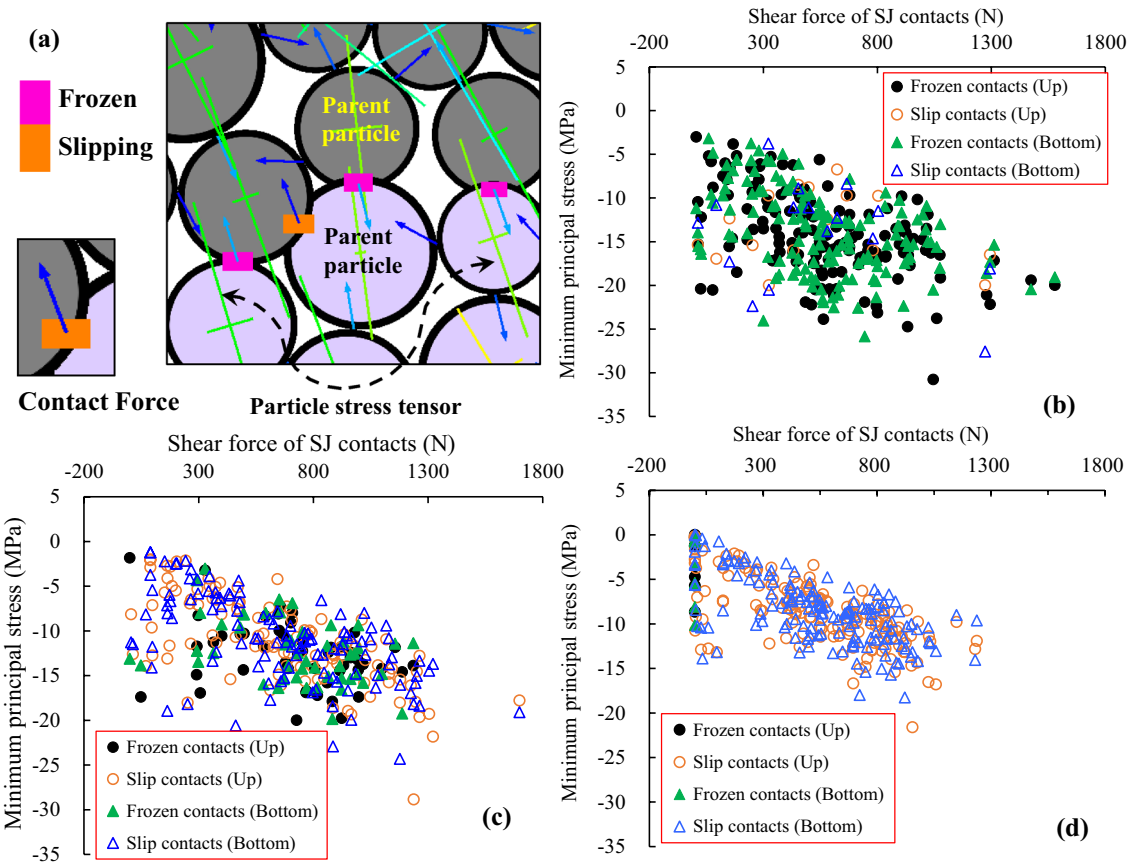

Fig. 15 **a** SJ contacts, contact forces, and calculated stress tensor on parent particles. Different colors of the particles signify balls belonging to the upper and lower blocks of the model (Fig. 1). Correlation between SJ shear force and corresponding minimum principal stress on parent particles for scenarios with normal stress for **a** 9 MPa (before peak normal load), **b** 7 MPa, and **c** 5 MPa. See Fig. 12 to identify the corresponding points in time (black dots)

was found between the planar joint surfaces, but this was not considered in our model. We believe that the smooth joints play a fundamental role in the shear behavior, but wear and associated gouge will affect the joint response.

6 Conclusions

This study presents a microscopic DEM-based model to simulate the frictional response of smooth joints under DNL. Although using simplified models, our simulations successfully reproduced the cyclic behavior of shear stress and apparent friction coefficient, the phase shift between peak shear stress and peak normal stress (peak shear stress delay), as well as between peak friction coefficient and peak normal stress (peak friction coefficient delay). α_s decreases with increasing normal loading rate and shear velocity. μ_a maximizes near the trough of the normal stress wave and minimizes at the crest. The maximum value of μ_a is nearly identical to the static friction coefficient. The minima of μ_a increase with normal loading rate and with decreasing shear velocity. α_f remains unchanged (~0.5), especially for cases with low shear velocities and low normal loading rates. The joint stiffness has a limited effect on the frictional behavior of the rock joints.

Although phase shift between peak shear stress and peak normal stress is a common phenomenon in direct shear tests under DNL conditions, the underlying mechanism of this phase shift has remained unclear so far. For the first time, we uncover the mechanism based on contact state changes and the evolutions of shear force, shear velocities, and shear displacement of individual contacts from a microscopic point of view. For cases with appropriate shear velocity (e.g., 0.003 m/s in this study), shear displacements at individual contacts quickly accumulate in the unloading stage, which results in more slipping contacts and continued growth of shear stress, although reduction of the normal stress takes place. As unloading continues, most of the joint contacts switch into the slipping state; thus, their shear forces do not depend on the slip increments but the imposed normal stress. However, for cases with very low or high shear velocities, the normal stress change dominates the evolution of shear

stress; therefore, no or only minor phase shift occurs. For cases with high shear velocity, most of the joint contacts are slipping during the whole process; hence, the shear forces depend on the normal force applied. For cases with very low shear velocity, most of the contacts are frozen, and tiny slip increments contribute only a little to the shear stress changes, i.e., normal load dominates the shear stress changes.

Stress distributions near the contacts indicate damage or failure in areas close to the joint; however, this phenomenon is only indicated in the simulations due to the unrealistic high strength parameters. Future studies are needed to investigate the stress heterogeneity-induced damage or failure very close to both sides of the rock joint.

The discrepancies between numerical simulations and laboratory experiments are mainly caused by the different types of dynamic excitation, some shortcomings in respect to the duplication of the micro-processes (e.g., 3D vs. 2D, evolution of real contact area, population, individual frictional strength, and their interaction), and the gouge between joint planes, which are not taken into account in the presented simulations. This study highlights the role of microscopic DEM models to investigate the frictional response of rock joints or faults under dynamic perturbations, and to study the underlying physics from a microscopic point of view, which is usually not possible in the laboratory. This study also suggests a critical need for further fundamental studies at the microscopic level.

Appendix

Compared with traditional shear tests (with constant normal load), totally different frictional behavior was observed. Experimental results showed that shear loads show cyclic behavior with a significant time shift between peak normal load and peak shear load (shear load delay), as shown in Fig. 16a. The relative time shift between peak normal load and peak shear load decreases with increasing dynamic amplitudes. The relative time shift between peak normal load and apparent friction coefficient (μ_a, defined as the ratio of actual shear stress to actual normal stress) is nearly constant (about a half cycle, μ_a delay), i.e., maxima of μ_a always occur at troughs of DNL. The maxima of μ_a are approximately equal to the static friction coefficient. The minima of μ_a always happen at crests of DNL, which decrease significantly with increasing dynamic amplitudes, as shown in Fig. 16b. Shear behavior also depends on shear velocities, as shown in Fig. 17. Peak shear loads increase as shear velocity rises. Peak shear loads lag behind peak normal loads, and the relative time shift increases with decreasing shear rates. The minima of μ_a could advance the crest of DNL but approach the crest with decreasing shear rate. The minima of μ_a increases as shear velocity rises.

The loading rate of DNL (i.e., normal load frequency) also affects the frictional behavior of the joint, as shown

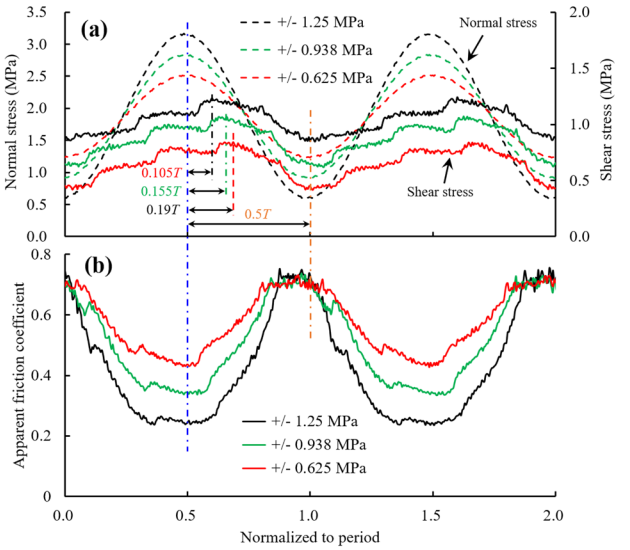

Fig. 16 Shear load and friction coefficient versus normalized period for several DNL tests with different dynamic load amplitudes. '*T*' means the period of the sinusoidal normal load. +/− 1.25 MPa signifies the sinusoidal normal load varies ± 1.25 MPa around the static normal stress level (i.e., the amplitude of the sinusoidal load is 1.25 MPa).

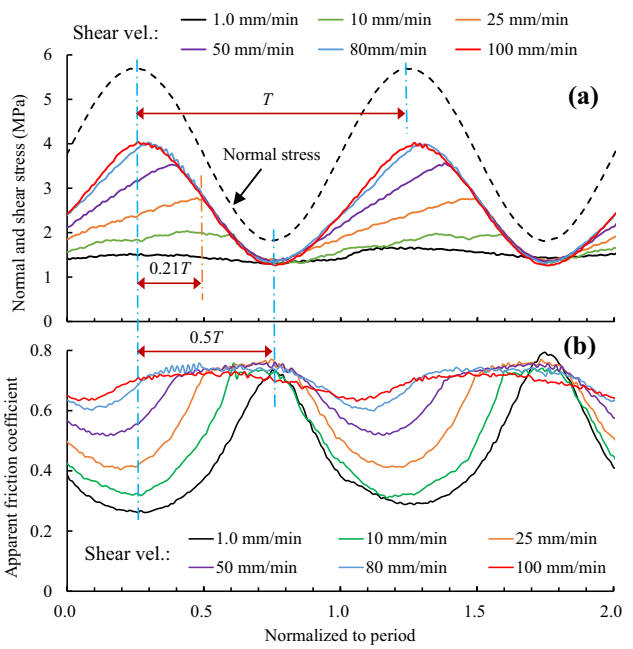

Fig. 17 Normal and shear stress as well as friction coefficient versus normalized period for several DNL tests with different shear velocity. '*T*' means the period of the sinusoidal normal load.

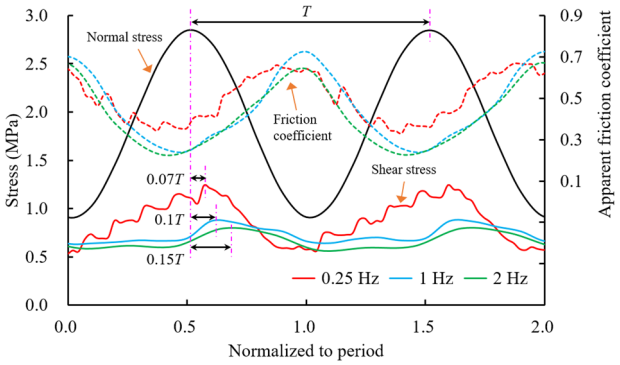

Fig. 18 Shear load and friction coefficient versus normalized period for several DNL tests with different frequency of DNL. '*T*' means the period of the sinusoidal normal load.

in Fig. 18. The maxima of the shear stress decrease as the normal load frequency increases (i.e., normal load rate increases), while the minima are roughly identical. The peaks of shear stress lag behind the peaks of normal stress, and the relative time shifts rise with increasing frequency. In the three tests, μ_a has the same waveform as the normal stress, but lags a half period behind the normal load, indicating normal stress frequency independence. μ_a maximizes at troughs of the normal stress, and the maxima roughly remain constant. μ_a minimizes at crests of normal stress, and minima slightly increase with decreasing frequency.

Acknowledgements Reviews from three anonymous reviewers significantly improved the manuscript. Financial support for this study is provided by the National Natural Science Foundation of China (No. 51704278). The first author (Q. Bai) also appreciates the Alexander von Humboldt Foundation for supporting his research in Germany.

References

Bahaaddini M, Sharrock G, Hebblewhite BK (2013) Numerical direct shear tests to model the shear behaviour of rock joints. Comput Geotech 51:101–115

Bai Q, Young RP (2020) Numerical investigation of the mechanical and damage behaviors of veined gneiss during true-triaxial stress path loading by simulation of in situ conditions. Rock Mech Rock Eng 53:133–151

Barthwal H, van der Baan M (2020) Microseismicity observed in an underground mine: Source mechanisms and possible causes. Geomech Energy Environ 22:100167

Ben-David O, Rubinstein SM, Fineberg J (2010) Slip-stick and the evolution of frictional strength. Nature 463:76–79

Bhat HS, Dmowska R, Rice JR, Kame N (2004) Dynamic slip transfer from the Denali to Totschunda faults, Alaska: testing theory for fault branching. Bull Seismol Soc Am 94:S202–S213

Capozza R, Vanossi A, Vezzani A, Zapperi S (2009) Suppression of friction by mechanical vibrations. Phys Rev Lett 103:085502

Cundall PA, Strack OD (1979) A discrete numerical model for granular assemblies. Géotechnique 29:47–65

Dang W, Konietzky H, Frühwirt T (2016) Direct shear behavior of a plane joint under dynamic normal load (DNL) conditions. Eng Geol 213:133–141

Dang W, Konietzky H, Frühwirt T (2017) Direct shear behavior of planar joints under cyclic normal load conditions: effect of different cyclic normal force amplitudes. Rock Mech Rock Eng 50:3101–3107

Dang W, Konietzky H, Chang L, Frühwirt T (2018) Velocity-frequency-amplitude-dependent frictional resistance of planar joints under dynamic normal load (DNL) conditions. Tunn Undergr Space Technol 79:27–34

Dang W, Konietzky H, Frühwirt T, Herbst M (2020) Cyclic frictional responses of planar joints under cyclic normal load conditions: laboratory tests and numerical simulations. Rock Mech Rock Eng 53:337–364

Dieterich JH, Kilgore BD (1994) Direct observation of frictional contacts: new insights for state-dependent properties. Pure Appl Geophys 143:283–302

Duan B, Oglesby DD (2005) Multicycle dynamics of nonplanar strike-slip faults. J Geophys Res Solid Earth 110:B03304

Ferdowsi B, Griffa M, Guyer RA, Johnson PA, Carmeliet J (2014) Effect of boundary vibration on the frictional behavior of a dense sheared granular layer. Acta Mech 225:2227–2237

Ferdowsi B, Griffa M, Guyer RA, Johnson PA, Marone C, Carmeliet J (2015) Acoustically induced slip in sheared granular layers: application to dynamic earthquake triggering. Geophys Res Lett 42:9750–9757

Fortin J, Millet O, de Saxcé G (2003) Construction of an averaged stress tensor for a granular medium. Eur J Mech A/Solids 22:567–582

Giacco F, Saggese L, de Arcangelis L, Lippiello E, Ciamarra MP (2015) Dynamic weakening by acoustic fluidization during stick-slip motion. Phys Rev Lett 115:128001

Greenwood JA, Williamson JP (1966) Contact of nominally flat surfaces. Proceedings of the royal society of London. Series A. Math Phys Sci 295:300–319

Griffa M, Daub E, Guyer R, Johnson P, Marone C, Carmeliet J (2011) Vibration-induced slip in sheared granular layers and the micromechanics of dynamic earthquake triggering. Europhys Lett 96:14001

Griffa M, Ferdowsi B, Daub E, Guyer R, Johnson P, Marone C, Carmeliet J (2012) Meso-mechanical analysis of deformation characteristics for dynamically triggered slip in a granular medium. Phil Mag 92:3520–3539

Griffa M, Ferdowsi B, Guyer R, Daub E, Johnson P, Marone C, Carmeliet J (2013) Influence of vibration amplitude on dynamic triggering of slip in sheared granular layers. Phys Rev E 87:12205

Harris RA (1998) Introduction to special section: Stress triggers, stress shadows, and implications for seismic hazard. J Geophys Res Solid Earth 103:24347–24358

Hobbs B, Brady B (1985) Normal stress changes and the constitutive law for rock friction. EOS Trans Am Geophys Union 66:382

Hong T, Marone C (2005) Effects of normal stress perturbations on the frictional properties of simulated faults. Geochem Geophys Geosyst 6:Q03012

Itasca Consulting Group Inc (2017) PFC manual, version 5.0, Minneapolis

Ivars DM, Pierce ME, Darcel C, Reyes-Montes J, Potyondy DO, Young RP, Cundall PA (2011) The synthetic rock mass approach for jointed rock mass modelling. Int J Rock Mech Min Sci 48:219–244

Johnson PA, Savage H, Knuth M, Gomberg J, Marone C (2008) Effects of acoustic waves on stick–slip in granular media and implications for earthquakes. Nature 451:57–60

Johnson PA, Carmeliet J, Savage H, Scuderi M, Carpenter B, Guyer R, Daub E, Marone C (2016) Dynamically triggered slip leading

to sustained fault gouge weakening under laboratory shear conditions. Geophys Res Lett 43:1559–1565
Kilgore B, Lozos J, Beeler N, Oglesby D (2012) Laboratory observations of fault strength in response to changes in normal stress. J Appl Mech 79:31007
Kilgore B, Beeler NM, Lozos J, Oglesby D (2017) Rock friction under variable normal stress. J Geophys Res Solid Earth 122:7042–7075
Konietzky H, Frühwirt T, Luge H (2012) A new large dynamic rockmechanical direct shear box device. Rock Mech Rock Eng 45:427–432
Kulatilake P, Malama B, Wang J (2001) Physical and particle flow modeling of jointed rock block behavior under uniaxial loading. Int J Rock Mech Min Sci 38:641–657
Lambert C, Coll C (2014) Discrete modeling of rock joints with a smooth-joint contact model. J Rock Mech Geotech Eng 6:1–12
Li Q, Tullis TE, Goldsby D, Carpick RW (2011) Frictional ageing from interfacial bonding and the origins of rate and state friction. Nature 480:233–236
Li C, Sun X, Wang C, Xu X, Xie B, Li J (2016) The correlated characteristics of micro-seismic and electromagnetic radiation signals on a deep blasting workface. J Geophys Eng 13:1020–1035
Li Z, Yu S, Zhu W, Feng G, Xu J, Guo Y, Qi T (2020) Dynamic loading induced by the instability of voussoir beam structure during mining below the slope. Int J Rock Mech Min Sci 132:104343
Linker M, Dieterich JH (1992) Effects of variable normal stress on rock friction: observations and constitutive equations. J Geophys Res Solid Earth 97:4923–4940
Mair K, Marone C (1999) Friction of simulated fault gouge for a wide range of velocities and normal stresses. J Geophys Res Solid Earth 104:28899–28914
Mehranpour MH, Kulatilake PH (2017) Improvements for the smooth joint contact model of the particle flow code and its applications. Comput Geotech 87:163–177
Müser MH, Dapp WB, Bugnicourt R, Sainsot P, Lesaffre N, Lubrecht TA, Persson BN, Harris K, Bennett A, Schulze K (2017) Meeting the contact-mechanics challenge. Tribol Lett 65:118
Ohnaka M (2013) The physics of rock failure and earthquakes. Cambridge University Press, Cambridge
Orlecka-Sikora B, Lasocki S, Lizurek G, Rudziński Ł (2012) Response of seismic activity in mines to the stress changes due to mining induced strong seismic events. Int J Rock Mech Min Sci 53:151–158
Park J-W, Song J-J (2009) Numerical simulation of a direct shear test on a rock joint using a bonded-particle model. Int J Rock Mech Min Sci 46:1315–1328
Pierce M, Cundall P, Potyondy D, Mas Ivars D (2007) A synthetic rock mass model for jointed rock, Rock mechanics: meeting society's challenges and demands, pp. 341–349
Potyondy DO (2015) The bonded-particle model as a tool for rock mechanics research and application: current trends and future directions. Geosyst Eng 18:1–28
Potyondy DO, Cundall PA (2004) A bonded-particle model for rock. Int J Rock Mech Min Sci 41:1329–1364
Prakash V (1998) Frictional response of sliding interfaces subjected to time varying normal pressures. J Tribol 120:97–102
Rubinstein S, Cohen G, Fineberg J (2006) Contact area measurements reveal loading-history dependence of static friction. Phys Rev Lett 96:256103
Saadat M, Taheri A (2020) A numerical study to investigate the influence of surface roughness and boundary condition on the shear behaviour of rock joints. Bull Eng Geol Environ 79:2483–2498
Savage HM, Marone C (2007) Effects of shear velocity oscillations on stick-slip behavior in laboratory experiments. J Geophys Res Solid Earth 112:B02301
Shreedharan S, Rivière J, Bhattacharya P, Marone C (2019) Frictional state evolution during normal stress perturbations probed with ultrasonic waves. J Geophys Res Solid Earth 124:5469–5491
Sobolev G, Spetzler H, Koltsov A, Cheldize T (1993) An experimental study of triggered stick-slip. Pure Appl Geophys 140:79–94
Sobolev G, Ponomarev A, Maibuk YY (2016) Initiation of unstable slips–microearthquakes by elastic impulses. Izvestiya Phys Solid Earth 52:674–691
Stein RS (1999) The role of stress transfer in earthquake occurrence. Nature 402:605–609
Stesky R, Hannan S (1987) Growth of contact area between rough surfaces under normal stress. Geophys Res Lett 14:550–553
Tang J-Z, Yang S-Q, Zhao Y-L, Tian W-L (2020) Experimental and numerical modeling of the shear behavior of filled rough joints. Comput Geotech 121:103479
Wang W, Scholz CH (1994) Micromechanics of the velocity and normal stress dependence of rock friction. Pure Appl Geophys 143:303–315
Xing H, Han Z (2020) Caving-induced fault reactivation behaviour and its effects on mining safety with a multiple seam context. Acta Geotech
Xing HL, Makinouchi A, Zhao C (2007) Three-dimensional finite element simulation of large-scale nonlinear contact friction problems in deformable rocks. J Geophys Eng 5:27–36
Ziegler M, Reiter K, Heidbach O, Zang A, Kwiatek G, Stromeyer D, Dahm T, Dresen G, Hofmann G (2015) Mining-induced stress transfer and its relation to a Mw 1.9 seismic event in an ultra-deep South African gold mine. Pure Appl Geophys 172:2557–2570